Fluidic phase–change materials with continuous latent heat from theoretically tunable ternary metals for efficient thermal management

Hua Wang[a,1], Yan Peng[a,1], Hao Peng[a], and Jiuyang Zhang[a,2]

Phase–change materials (PCMs), as important energy storage materials (ESMs), have been widely used in heat dissipation for electronics. However, PCMs are encountering huge challenges since the extremely limited space in microelectronics largely suppresses the applied volume of PCMs, which demands excellent PCMs that can fully utilize the valuable latent heat. This work successfully found a universal strategy toward powerful ESMs from fluidic ternary metals (TMs, GaInSn as a representative TM in this work). TMs exhibit high thermal conductivity (20.3 W m^{-1} K^{-1}) and significantly effective latent heat (115 J/cm^3) and, more important, show continuous phase transition and full utilization of the valuable latent heat. Interestingly, theoretical prediction through ternary phase diagram is carried out to easily tune the melting range, latent heat, and fluidity (viscosity) of TMs to adapt with different service conditions. As a result, thermally conductive silicone grease can be conveniently fabricated via simple shear mixing of TM and polymers. Such thermally conductive TM grease inherits the merits of TM, exhibiting continuous thermal control over daily electronics according to thermal shock performance.

phase change materials | thermal management | liquid metals | electronics | ternary metals

Energy storage technologies have received lots of attention from integrated circuits and the modern electronic industry (1, 2) because they can provide excellent thermal control over the system to improve reliability and extend the service life of electronics. As important energy storage materials (ESMs), phase–change materials (PCMs) have been widely used in the field of heat dissipation for electronics due to the endothermic characteristics of phase transition (3–8), which can efficiently route thermal energy away and maintain the system temperature within a suitable temperature range. However, as the rapid development of high-powered devices and modern microelectronics continues (9–11), traditional PCMs cannot meet the increasing demands from the industry (12–16). For example, PCMs (such as paraffin, polyols, and fatty acids) are notorious for their very low thermal conductivity ($\kappa < 0.5$ W m^{-1} K^{-1}) (15–17), which greatly hinders their practical applications in advanced electronic devices. In addition, today's microelectronics are becoming more and more miniaturized (2, 14, 18–23). For example, the size of the central processing units (CPUs) in cell phones and other personal devices rapidly decreased from about 100 mm^2 to 70 mm^2 in 5 years, leaving limited space for thermal materials to be utilized among the CPU, die, and thermal spreader. As a result, due to the extremely limited space, the volume of PCMs that can be applied in microelectronics is largely suppressed, leading to poor thermal control in highly compact electronics. Furthermore, the limited amount of PCMs in microdevices asks for full use of the latent heat in the most desired situation. However, most latent heat of PCMs is ineffective and wasted in microelectronics since their phase transitions have to be completed around their fixed melting points, causing the loss of continuous and precise thermal control over complicated industrial systems under large temperature variations (24).

To address the above critical issues, low-melting-point alloys (LMPAs) have been considered as alternative choice for microelectronics because they possess excellent thermal conductivity and, more important, high latent heat per unit volume (24–26). Unfortunately, similar to many PCMs (e.g., stearic acids), such latent heat can only be released around their eutectic temperatures, showing poor adaptability to large environmental temperature variations, thus limiting their thermal control over different electronic systems. For example, liquid metal, gallium (Ga), has been used as a successful thermally conductive PCM in electronics due to its low toxicity, room temperature fluidity, high thermal conductivity, and low melting point ($T_m = 29.8 °C$) (27–29). However, the service temperature of most electronics is above this melting temperature

Significance

This work brings the knowledge of classic ternary-phase transitions of metals into the field of energy storage materials (ESMs), providing a powerful and universal strategy toward high-performance ESMs. Compared with traditional phase–change materials (PCMs), the phase transition temperature range and latent heat of the ternary metals (TMs) can be theoretically controlled via their compositions. The TMs exhibit unique advantages over previous PCMs, including excellent environmental adaptability, continuous phase transition, high thermal conductivity, and remarkable latent heat. The thermal grease based on fluidic TM is conveniently fabricated. The TM grease shows excellent performance for daily electronics upon thermal shock characterizations. This work should have broad and significant impact in the field of thermal industry, electronics, and energy materials.

[1]H.W. and Y.P. contributed equally to this work.

[2]To whom correspondence may be addressed. Email: jiuyang@seu.edu.cn.

(30), and Ga is already in a liquid state and thus has little control over the devices' temperature due to its narrow solid–liquid phase transition range. As a result, most current liquid metal (Ga and its alloys)–based thermal materials in consumer electronics are applied as thermal interface materials, e.g., liquid metal thermal paste/gels for the Sony PlayStation, utilizing the excellent thermal conductivity instead of their latent heat (31). Therefore, a unique type of LMPAs needs to be designed whose latent heat can be precisely controlled during the entire working time of microelectronic systems, which will realize the advantages (i.e., excellent environmental adaptability, continuous phase transition, effectively latent heat, and high thermal conductivity) of such special LMPAs as excellent ESMs.

This work successfully found a universal strategy that created such phase–change ESMs from fluidic and theoretically tunable ternary metals (TMs). In contrast with traditional PCMs with a single melting point, fluidic TMs (gallium-indium-tin [$Ga_xIn_ySn_z$] as representative metals in this work; x, y, and z refer to the atomic percentage in TMs) show a unique broad melting temperature range from 10 °C to 100 °C. TMs exhibit continuous phase transition in this broad temperature range without sacrificing their latent heat per unit volume (115 J/cm³) and thermal conductivity (20.28 W m⁻¹ K⁻¹). Interestingly, the ternary phase diagram provides a convenient way to theoretically predict and tune the melting range and latent heat of TMs, which makes the full and effective utilization of the latent heat (effective latent heat) in different electronics with large environmental temperature variation. Notably, TMs are fluidic under mild temperature conditions (> 10 °C), and the viscosity of TMs can also be precisely mediated according to their phase diagrams via temperature and composition. As a result, thermally conductive silicone grease can be conveniently fabricated via simple shear mixing of TM and polymers. Surprisingly, the as-prepared grease successfully inherits the merits of TM, exhibiting continuous phase transition, effective latent heat, and high thermal conductivity up to 7.5 W m⁻¹ K⁻¹, much higher than most commercially available products (κ = 0.7–5 W m⁻¹ K⁻¹). Thermal shock results on daily electronics (such as LED and CPUs) demonstrate that TM silicone grease exhibits superior capability in thermal energy removal compared with Ga and commercially available products. This work utilizes the phase transition of ternary metals in the field of ESMs, providing a universal principle for powerful ESMs (not limited to Ga alloys) with excellent environmental adaptability, high thermal conductivity, continuous phase transition, and significantly effective latent heat.

Results and Discussion

The heat dissipation is one of the most critical issues for electronics that limits their lifetime, high performance, and miniaturized design. For example, in a running computer, the CPU (Intel Core i5-7200U) always has the highest temperature on the motherboard, as shown in Fig. 1A. Specifically, we recorded the temperature of a CPU in Fig. 1A with time. Under normal working conditions, the temperature of a CPU is generally > 60 °C (as recorded by software in Fig. 1B). The temperatures of daily consumer electronics are plotted in Fig. 1C, and their normal working temperatures range from 30 °C to 70 °C (32–34). Tang et al. recently provided profound studies for the phase behavior of Ga and its alloys (35). Although Ga and its derivatives have been broadly applied as effective ESMs due to their phenomenal thermal conductivities and feasible latent heat per unit volume, the phase transition temperature of Ga-based materials is approximately 30 °C, lower than the

service temperature of most consumer electronics. Therefore, if the pure Ga-based ESMs are applied for daily consumer electronics, then the latent heat will be wasted and ineffective to control their temperatures under common working conditions. The narrow melting range means that the latent heat of Ga can only be used in limited situations. Considering the great difference for many electronic devices, a PCM grease with a large melting temperature range is preferable. In contrast, binary metals (BM) and TMs have a broad melting range instead of a single melting point. As shown in Fig. 1D, the melting process of Ga is completed around its fixed melting point (29.8 °C). However, BMs and TMs are greatly different from Ga, showing a continuous process in a broad melting range, which was also observed in classical semisolid metal processing (36, 37). It can be observed that BM starts to melt at approximately 30 °C and gradually transitions into liquid until 80 °C. Similarly, TM starts to melt at 30 °C and completes the melting process at 80 °C. To demonstrate the impact of such continuous melting on temperature control, the temperature changes of different metals (Ga, BM, and TM) were recorded with time under adiabatic heating as shown in Fig. 1E. The temperature of Ga exhibited a plateau near 30 °C corresponding to its melting point but increased rapidly after melting. It should be noted that in TM and BM, this melting process is actually an endothermic melting process in which solid fractions gradually dissolve in liquid phases. However, due to the continuous phase transition feature of BM and TM, there is no platform in their temperature curves. In contrast, their temperatures rise slowly, and a turning point appears at 70 °C, corresponding to their liquidus in the phase diagram (fully discussed in Fig. 2).

As shown in Fig. 1C, the service temperatures of common electronics are > 30 °C. Therefore, we replotted Fig. 1E starting from 30 °C to show the effective thermal control in the window of the service temperature range for the system (Fig. 1F). It can be observed that the temperature of Ga rises at the fastest rate of 0.18 °C/s upon heating, showing the worst ability of temperature control. On the contrary, TM has the lowest increasing rate of temperature at 0.07 °C/s because it continuously absorbs heat through continuous phase transition above 30 °C, exhibiting the best performance of temperature management. For BM, the rates of temperature increase (0.12 °C/s of BM_1 ($Ga_{0.82}Sn_{0.18}$) and 0.10 °C/s of BM_2 ($Ga_{0.50}In_{0.50}$)) are higher than that of TM but lower than for Ga. The continuous phase transition can be further confirmed by dynamic scanning calorimetry (DSC). As shown in Fig. 1G, there is only one endothermic peak of Ga, indicating its phase transition at 29.8 °C. However, two endothermic peaks are observed in the DSC results for BM and TM, corresponding to two different melting (endothermic melting) stages in these metals. The first sharp melting peak is associated with the phase transition from solid phase to the solid–liquid biphasic state, while the second broad melting peak corresponds to the gradual transition from the biphasic state to the liquid phase. The broad peak in the second stage clearly indicates the continuous phase transition and continuous absorption of heat by TM and BM in a broad temperature range above 30 °C. Notably, although TM and BM have a unique continuous phase transition, they do not sacrifice the merits of the distinguished fluidity and phenomenal thermal conductivity (19.40 W m⁻¹ K⁻¹ of BM_1, 21.29 W m⁻¹ K⁻¹ of BM_2 and 20.28 W m⁻¹ K⁻¹ of TM, Fig. 1I) as does broadly applied Ga (19.77 W m⁻¹ K⁻¹) in industrial thermal management. The continuous melting enthalpy of different metals above 30 °C can be calculated by the integrated shaded area of the enlarged DSC curves (Fig. 1H). As shown in
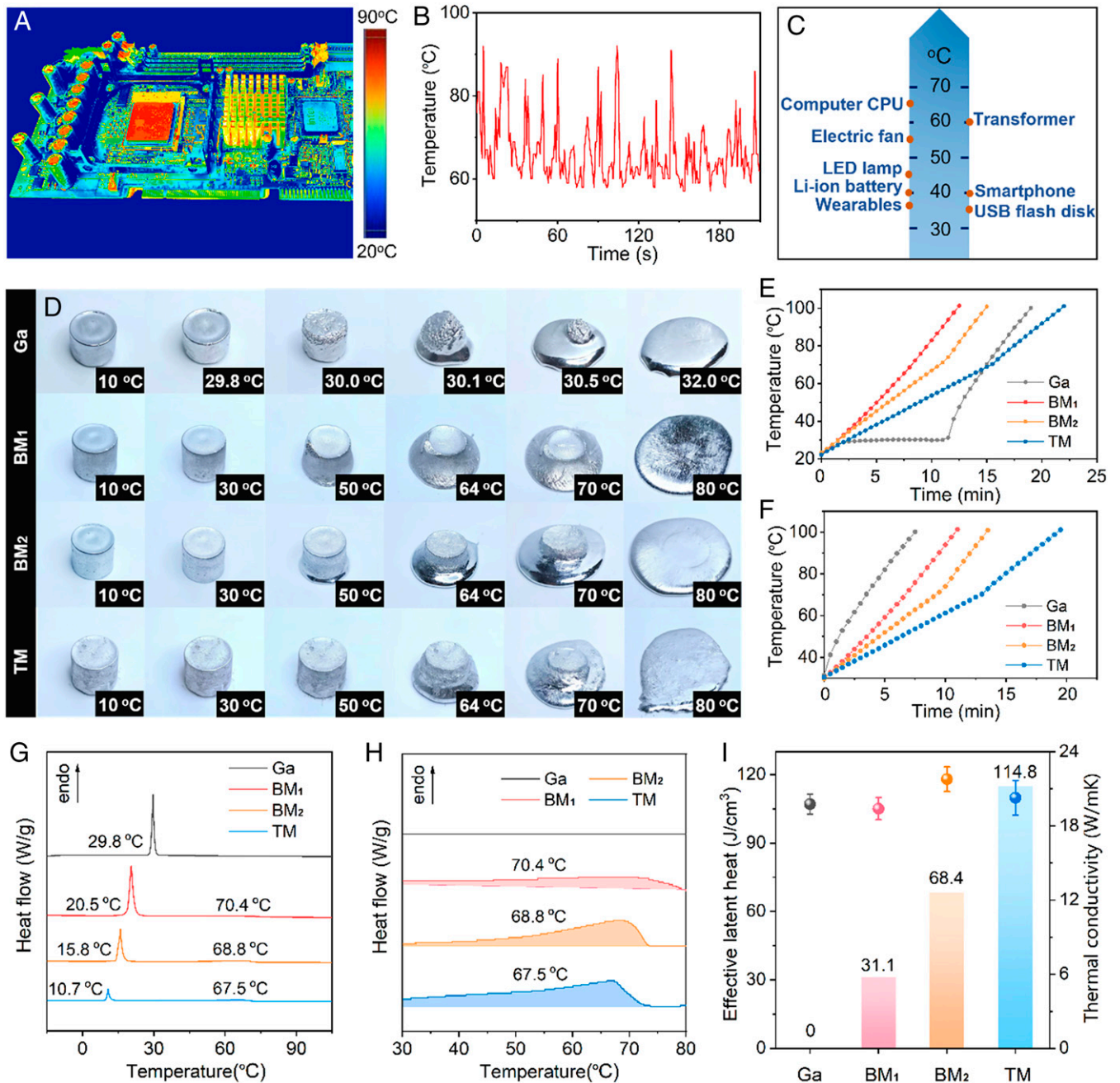
Fig. 1. Service temperatures for daily electronics and the continuous latent heat from BMs and TMs. (*A*) Temperature distribution for a working computer motherboard. The CPU has the highest temperature. (*B*) The recorded temperature for a normal working CPU (Intel Core i5-7200U) with time. (*C*) The service temperatures of consumer electronics. (*D*) Photos for the melting process of Ga, the BM $Ga_{0.82}Sn_{0.18}$ (BM$_1$), $Ga_{0.50}In_{0.50}$ (BM$_2$), and the TM $Ga_{0.20}In_{0.46}Sn_{0.34}$ (TM). (*E*) Temperature changes of different metals (2 mL) under an adiabatic heating process (heated by a 4W heating mantle). (*F*) The temperature–time plot starting from 30 °C for different metals from *E*. (*G*) DSC heating curves for different metals from −15 °C to 105 °C at 2 °C/min. There are two peaks in the DSC curves for BM and TM, corresponding to the two stages of the phase transitions. 'endo' indicates 'endothermal'. (*H*) Enlarged part of the DSC heating curves in the second melting stage, and the enthalpy of fusion (latent heat) can be calculated from the integration of the shadowed areas. 'endo' indicates 'endothermal'. (*I*) The effective latent heat (columns) and thermal conductivity (dots) of different metals. Here, the effective latent heat is the enthalpy actually used for working devices.

Fig. 1*I*, in the second melting stage, the effective latent heat of Ga, BM$_1$, and BM$_2$ are 0 J/cm^3, 31.1 J/cm^3, and 68.4 J/cm^3, respectively. In contrast, TM has the highest effective latent heat of 114.8 J/cm^3, far beyond that of Ga and 60% higher than that of BM. With high effective latent heat and high thermal conductivity, TM can be a very powerful ESM for common electronics to match their general service temperatures.

To fully understand the phase transition behaviors of these metals and provide a theoretical prediction of the thermal performance of different metals, the step cooling experiments and theoretical analysis of phase diagrams for Ga, BM ($Ga_{0.50}In_{0.50}$), and TM ($Ga_{0.40}In_{0.28}Sn_{0.32}$) are shown in Fig. 2. The step cooling curve of Ga (Fig. 2*A*) shows that Ga only has a single liquid–solid phase transition point at 30 °C, consistent with DSC results (*SI Appendix*, Fig. S1), while BM ($Ga_{0.50}In_{0.50}$) has two phase transitions. One of these, at 70 °C, is associated with the transition of indium (In) from a liquid to a solid state. The X-ray diffraction (XRD) patterns below and above 70 °C clearly show the phase transition at 70 °C (*SI Appendix*, Fig. S2). The other phase transition is at 15.5 °C, corresponding to the complete solidification of Ga and In, which is also confirmed by XRD patterns (*SI Appendix*, Fig. S2). Meanwhile, the step cooling and XRD patterns of BM ($Ga_{0.82}Sn_{0.18}$) are
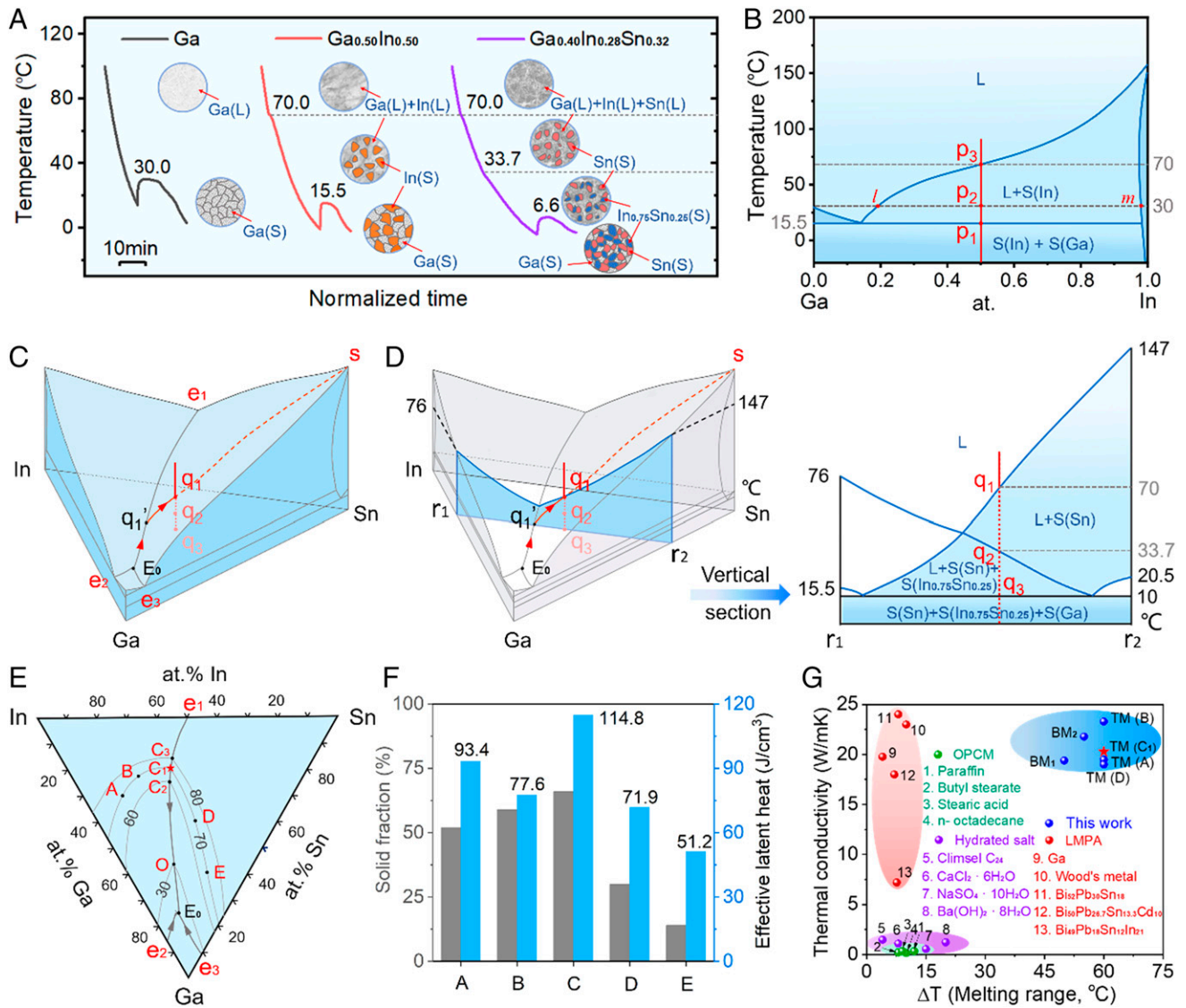
Fig. 2. The phase transition of BMs and TMs. (*A*) Step–cooling curves of Ga, BM ($Ga_{0.50}In_{0.50}$), and TM ($Ga_{0.40}In_{0.28}Sn_{0.32}$) (turbulence in the end of each curve is due to supercooling of Ga). The insets show the phases of the metals under different temperatures. L: liquid phase; S: solid phase. (*B*) Ga-In binary phase diagram. p_1 and p_3 correspond to the liquidus temperature of 70 °C and the solidus temperature of 15.5 °C for $Ga_{0.50}In_{0.50}$. The l and m are intersectional points between the liquidus line/solidus line and isothermal lines (30 °C), respectively. (*C*) Ga-In-Sn ternary phase diagram. E_0: ternary eutectic point (10 °C); e_1E_0, e_2E_0, e_3E_0: the eutectic curves of the system; q_1': the intersection of e_1E_0 and the extension of the sq_1 line. The liquid composition of TM ($Ga_{0.40}In_{0.28}Sn_{0.32}$) changes along $E_0q_1'q_1$ with heating from 10 °C to 70 °C. q_1, q_2, and q_3 on the same vertical line are the phase transition points for TM ($Ga_{0.40}In_{0.28}Sn_{0.32}$) during heating shown in *D*. (*D*) Vertical section of the ternary phase diagram parallels to the In-Sn face through q_1, q_2, and q_3. In (*C*) and (*D*), 's' is the point on the liquidus surface for the pure Tin. The section shows the detailed phase transition for the TM ($Ga_{0.40}In_{0.28}Sn_{0.32}$) from q_3 to q_1 during heating. (temperatures in the section are calculated as shown in *SI Appendix*, Fig. S9). (*E*) The liquidus projection of the Ga-In-Sn system with eutectic curves and liquidus curves of 30 °C, 60 °C, 70 °C, and 80 °C. (A, B, D, and E are points on the liquidus curves of 70 °C; O, C_2, C_1, and C_3 are intersections of the eutectic curve e_1E_0 and the liquidus curves of 30 °C, 60 °C, 70 °C, and 80 °C, respectively). A phase diagram of Ga-In-Sn with all eutectic lines is shown in *SI Appendix*, Fig. S10. (*F*) The molar solid fractions (gray columns) and effective latent heat (blue columns) calculated from DSC results (*SI Appendix*, Fig. S11) of the metals corresponding to A ($Ga_{0.30}In_{0.57}Sn_{0.13}$), B ($Ga_{0.23}In_{0.55}Sn_{0.22}$), C_1 ($Ga_{0.20}In_{0.46}Sn_{0.34}$), D ($Ga_{0.40}In_{0.28}Sn_{0.32}$), and E ($Ga_{0.60}In_{0.13}Sn_{0.27}$) above 30 °C. (*G*) The thermal conductivity versus the melting range of different PCMs from references (17, 25) with melting temperatures below 100 °C. The melting range of PCMs in this work is 30 °C to 70 °C with the highest effective latent heat of 114.8 J/cm³, while the melting range of conventional PCMs (except paraffin, $Na_2SO_4 \cdot 10H_2O$, and $Bi_{49}Pb_{18}Sn_{12}In_{21}$) is not exactly within the range of 30 °C to 70 °C, and the effective latent heat available is very low (close to zero).

similar to those of BM ($Ga_{0.50}In_{0.50}$) (*SI Appendix, Fig. S3*). However, the cooling curve of TM ($Ga_{0.40}In_{0.28}Sn_{0.32}$) is more complicated due to the three gradients in the system. The first turning point is at 70 °C due to the precipitation of tin (Sn) from the liquid. Then at 33.7 °C, the second phase transition happens due to the coprecipitation of the $In_{0.75}Sn_{0.25}$ and Sn blends, which enables a three-phase coexisting state, consistent with the DSC results (*SI Appendix, Fig. S1*). Finally, the solvent Ga and the solute ($In_{0.75}Sn_{0.25}$ and Sn blends) cosolidify below 6.6 °C. Similar to BM, the three stages of phase transition for TM can be also verified by XRD patterns (*SI Appendix, Fig. S4*).

From the cooling results for metals discussed in Fig. 2*A*, we found that the phase transition for Ga is only approximately 30 °C, which means that the latent heat of phase transition for pure Ga-based ESMs does not contribute to thermal management for most electronics with service temperatures above 30 °C. Compared with pure Ga, BM and TM have continuous phase transitions above 30 °C, suitable for daily electronics. However, in contrast with pure Ga, since the number of constituents in BMs and TMs increases, a question is be raised regarding how to theoretically determine the composition of BM or TM to exhibit the best performance for thermal management. Fortunately, phase

diagrams of BM and TM provide strong support to address this issue. Fig. 2B is the Ga-In binary phase diagram (38, 39), and the dashed lines show the isotherms of 30 °C and 70 °C, corresponding to the lower and upper limits of the service temperature for daily electronics. Surprisingly, when the composition has a liquidus temperature of exactly 70 °C, it will have the largest effective latent heat to maintain the temperature of electronics below their upper limit temperature (70 °C). For example, BM ($Ga_{0.50}In_{0.50}$) has the liquidus temperature exactly at 70 °C. When BM ($Ga_{0.50}In_{0.50}$) is heated from p_1 to p_3 (vertical line in Fig. 2B), it will have one phase transition at p_1 (15.5 °C), corresponding to the melt of Ga. From p_1 to p_2, In gradually dissolves in Ga. However, the latent heat of the phase transition below p_2 (30 °C) usually does not contribute to the cooling of the electronics due to the lower limit of the service temperature at 30 °C (40). The continuous phase transition from p_2 to p_3 makes substantial contributions to the system above 30 °C. Therefore, the effective latent heat contributes to the cooling of electronics starting from p_2 to p_3. According to the lever rule in the phase diagram (40), when BM ($Ga_{0.50}In_{0.50}$) is heated in the service temperature window for daily electronics from p_2 (30 °C) to p_3 (70 °C), the molar fraction of solid indium that transits into liquid can be calculated as lp_2/lm = 39%, indicating a theoretical latent heat of 73.1 J/cm³, which is basically consistent with the DSC experimental value in Fig. 1I. Detailed calculation is shown in *SI Appendix*, Fig. S5. In a similar way, when the BM has liquidus temperatures at 60 °C ($Ga_{0.64}In_{0.36}$) and 80 °C ($Ga_{0.36}In_{0.64}$), the theoretical latent heat from 30 °C to 70 °C can be predicted as 40.3 J/cm³ and 53.7 J/cm³ (detailed calculation can be found in *SI Appendix*, Fig. S5). The results show that BM ($Ga_{0.50}In_{0.50}$) with a liquidus temperature of 70 °C has the largest solid fraction (39%) and latent heat (73.1 J/cm³) in the service temperature window for for daily electronics from 30 °C to 70 °C. In contrast, BMs with liquidus temperatures at 60 °C and 80 °C show solid fraction and latent heat at 22% and 28%, and 40.3 J/cm³ and 53.7 J/cm³, respectively. These results show that for BMs, when the liquidus temperatures of the composition match with the upper limit of the service temperature, they will provide the highest effective latent heat for cooling the system.

For TMs, we can figure out the best composition for different systems in a manner similar to BMs. However, the ternary phase diagram (*SI Appendix*, Fig. S8) is more complicated and is composed of three binary phase diagrams of Ga-In (Fig. 2B), Ga-Sn (*SI Appendix*, Fig. S6) (41), and In-Sn (*SI Appendix*, Fig. S7) (42, 43). As shown in Fig. 2C, a ternary eutectic point E_0 is observed in the Ga-In-Sn system, corresponding to the ternary eutectic temperature (10 °C) of TM. e_1E_0, e_2E_0, and e_3E_0 are the eutectic curves of the system. Similar to BM ($Ga_{0.50}In_{0.50}$), $Ga_{0.40}In_{0.28}Sn_{0.32}$ with a liquidus temperature of 70 °C was chosen to further study the phase transition process during heating. As shown in Fig. 2C, when TM ($Ga_{0.40}In_{0.28}Sn_{0.32}$) is heated from 30 °C to 70 °C, the composition of its liquid phase composition will change along the line of $E_0q_1'q_1$. The system of TM will go through q_1, q_2, and q_3 on the same vertical line—these are the turning points of phase transition. To further elucidate, Fig. 2D shows a vertical section for the composition ($Ga_{0.40}In_{0.28}Sn_{0.32}$) (the temperatures in the section are determined as shown in *SI Appendix*, Fig. S9). Upon heating, the solid phase (S(Sn) + S($In_{0.75}Sn_{0.25}$) + S(Ga)) of TM melts into liquid, corresponding to q_3 (10 °C). Then In and Sn continue to dissolve into the solvent until q_2 (33.7 °C). From q_2 to q_1 (70 °C), only Sn gets dissolved, and after q_1, the solid phase becomes completely liquid.

In order to find the optimal composition as the BM does, we plotted the liquidus projection for the ternary phase diagram with isotherms. For a clear view of the trending and explanation, the detailed TM phase diagram is shown in *SI Appendix*, Fig. S10 with an additional eutectic line. For the samples near the eutectic line, the small deviation in the composition has a significant impact on the phase transition and latent heat. Fig. 2E offers the liquidus projection with eutectic and liquidus curves of 30 °C, 60 °C, 70 °C, and 80 °C, respectively. Different from BM, the composition of TM is not fixed on the liquidus line of 70 °C. To figure out which point in the liquidus line has the highest solid fraction as well as effective latent heat, five representative compositions—A ($Ga_{0.30}In_{0.57}Sn_{0.13}$), B ($Ga_{0.23}In_{0.55}Sn_{0.22}$), C_1 ($Ga_{0.20}In_{0.46}Sn_{0.34}$), D ($Ga_{0.40}In_{0.28}Sn_{0.32}$), and E ($Ga_{0.60}In_{0.13}Sn_{0.27}$)—are marked on the 70 °C liquidus curve. Note that the A composition requires very careful preparation since it is quite close to one eutectic line shown in the detailed phase diagram (*SI Appendix*, Fig. S10). Interestingly, similar to the principle of BM, when the TM has a liquidus temperature of 70 °C, it has the largest effective latent heat (*SI Appendix*,). Specifically, for the varied compositions in the liquidus curve (70 °C), the intersection of the liquidus line with the eutectic curve has the best performance; that is, the point C_1. The point C_1 ($Ga_{0.20}In_{0.46}Sn_{0.34}$) has the largest practical latent heat because it has the highest solid fraction from 30 °C to 70 °C based on the lever rule in the ternary phase diagram (*SI Appendix*). The solid fractions of A, B, C_1, D, and E are calculated as 51%, 59%, 66%, 30%, and 14%, respectively. Their effective latent heat is obtained from their DSC curves (detailed procedure on choosing baseline and peak integration can be seen in *SI Appendix*, Figs. S11 and S12) as shown in Fig. 2F, which are consistent with their corresponding solid fractions. Although the solid fraction at point B is higher than at point A, the effective latent heat is lower than that at point A due to the peritectic reaction between Sn and In at point B, which will decrease the latent heat (40). The result can also be confirmed by the test under an adiabatic heating process as shown in *SI Appendix*, Fig. S13. In addition, the thermal conductivity of A, B, D, and E was also measured as exhibited in *SI Appendix*, Fig. S14. Furthermore, C_2 ($Ga_{0.24}In_{0.44}Sn_{0.32}$) and C_3 ($Ga_{0.15}In_{0.48}Sn_{0.37}$) are intersections between the liquidus lines of 60 °C, 80 °C, and the eutectic curve e_1E_0. As shown in *SI Appendix*, Fig. S15, the solid fractions of C_2 and C_3 from 30 °C to 70 °C can be calculated as 55% and 51% by the same method, and their effective latent heat is 102.8 J/cm³ and 91.5 J/cm³ from the DSC curves (*SI Appendix*, Fig. S16), respectively (*SI Appendix*). Overall, C_1 ($Ga_{0.20}In_{0.46}Sn_{0.34}$) has the largest effective latent heat for the thermal management of electronics because it has the highest solid fraction from 30 °C to 70 °C. The conclusion for TMs is consistent with that for BMs. That is, the metal should form a homogeneous single-phase alloy at the maximum service temperature and contain the highest possible fraction of solids at a lower service temperature while still being fluidic to enable processing. Note that such a conclusion is not only limited to Ga-In-Sn TMs. When the industry needs high working temperatures, one can follow this principle to find the phase diagram of new metals to determine the most suitable compositions to adapt with the system. However, the maximum effective latent heat of 114.8 J/cm³ for TM in this work is much larger than that of BM (68.4 J/cm³) due to the higher solid fraction of TM in the service temperature window of the system. In addition, Fig. 2G shows a comparison for the thermal conductivity and melting range of BMs and TMs in this work with previously reported organic and inorganic thermal storage

PCMs and LMPAs with melting temperatures below 100 °C (17, 25). It can be clearly seen that BMs and TMs in this work have the highest conductivity, largest melting range, and high effective latent heat in the working temperature range for the thermal management of electronics.

Considering the intriguing physical properties including large effective latent heat, continuous phase transition, and high thermal conductivity, TMs are highly suitable for powerful ESMs for different industrial and electronic systems. Interestingly, TMs are also fluidic under room temperature. Such fluidic TMs can be conveniently shear-mixed with polymers as room temperature liquid metals which their composites have been broadly applied in current thermal management industry (44, 45). Such convenient shear-mixing enables the convenient fabrication of composites for advanced ESMs based on TMs. We chose polydimethylsiloxane (DOW PMX200), the most commonly used composite in thermal control materials, to mix with TMs. The thermal grease is conveniently fabricated by mixing silicone oil with TMs ($Ga_{0.20}In_{0.46}Sn_{0.34}$, liquidus line at 70 °C) as shown in Fig. 3A. Ruan et al. reported that to effectively improve compatibility and reduce the thermal barrier, the chemical modification of fillers and polymer is necessary (46). The surface of metals is treated with silane coupling agents (hexadecyl trimethoxysilane) (*SI Appendix*, Figs. S17 and S18). Fourier transform-infrared spectrometry (FT-IR) confirms the successful surface modification of TMs. As shown in Fig. 3E, only the absorption peak of −OH at 3,450 cm^{-1} is found in the spectrum of pristine TM. However, the modified TM shows the characteristic peaks of the −CH$_3$ group at 2,925 cm^{-1} and the −CH$_2$− group at 2,854 cm^{-1}, consistent with the FT-IR of the coupling agent (47). In addition, the peaks in the FT-IR spectrum at 1,092 cm^{-1} and 1,635 cm^{-1} correspond to the stretching vibration peak of the Si−O−Si bond in silane and the H−O−H bending vibration peak (48), respectively. As control samples, Ga and BMs are also successfully modified as verified by FT-IR spectra (*SI Appendix*, Fig. S19). The modified TMs are highly compatible with silicone polymers, and the maximum volume fraction of the metals in the composites can reach as high as 80%. Scanning electron microscopy images (Fig. 3B) and elemental mapping results (*SI Appendix*, Fig. S20) show that the metal particles are homogeneously dispersed in polymers with an average diameter of 20 ± 10 μm (Fig. 3B). It is well known that the leaking issue is a severe disadvantage in the application of room-temperature liquid metal–based ESMs (49). Compared with room-temperature liquid metals, TM grease avoids the risk of leakage because the viscosity of TM is approximately 10^4 Pa•s (*SI Appendix*, Fig. S21), which can be conveniently tuned by adjusting the solid phase content based on the ternary phase diagram. Fig. 3 C and D present the outlook of TM grease and Ga grease coated on the aluminum plate. It can be seen that although the metal content is 80 vol%, TM grease is uniformly coated on the aluminum plate, while the leakage of liquid Ga in Ga grease was clearly observed during the coating procedure. In addition, both BM$_1$ grease and BM$_2$ grease are concomitant with a small amount of leakage, which is caused by their different liquid phase contents in the metals (*SI Appendix*, Fig. S22).

DSC measurements are utilized to characterize the thermal behavior of different greases based on Ga, $Ga_{0.82}Sn_{0.12}$ (BM$_1$), $Ga_{0.50}In_{0.50}$ (BM$_2$), and TM. As shown in Fig. 3F and *SI Appendix*, Fig. S23, the introduction of polymer has no obvious effect on the phase transition and latent heat for all the metals. In particular, the behavior of the continuous phase transition for these thermal greases in the service temperature window

(30 °C to 70 °C) is successfully inherited from their corresponding metals (*SI Appendix*, Fig. S24 and Fig. 3G). Similar to pure Ga, Ga grease has no effective latent heat above 30 °C. TM grease still exhibits the largest latent heat, 3.4 and 1.6 times higher than that of BM$_1$ and BM$_2$ grease, respectively, providing significant performance for their subsequent thermal management. The thermal conductivity of these greases at room temperature is measured as shown in Fig. 3H. The presence of interfaces between the polymer and metal after mixture reduces the thermal conductivity compared with pure metals. Fig. 3H indicates that the apparent thermal conductivity of TM grease is positively correlated with metal content. When the metal content is 80 vol%, the thermal conductivity is as high as 7.5 W m^{-1} K^{-1}, which is much higher than that of most commercially available phase–change ESMs (κ = 0.7 to 5 W m^{-1} K^{-1}) and is close to that of liquid metal composites reported in the literature (50, 51). Interestingly, the thermal conductivity of TM grease varies at different temperatures. As shown in *SI Appendix*, Fig. S25, when the temperature exceeds 70 °C, the thermal conductivity of TM grease decreases to 5.5 ± 0.25 W m^{-1} K^{-1}, which is because TM changes from a solid–liquid coexistence to a complete liquid state at 70 °C. More important, electronics usually work in the form of thermal shocks. In a short time, a large heat flux will be generated in electronics due to the fluctuation in the power supply or application program (e.g., CPU sharp increasing usage). Therefore, ESMs must have the ability to withstand many cycles of transient thermal shock. Fig. 3I shows the temperature of 80 vol% Ga grease and 75 vol% TM grease under the same thermal shock for 15 cycles. The thermal shock is performed by heating the grease for 30 s at the same power (a 2.2 W mantle) and then cooled naturally, simulating the common performance in electronics. The results indicate that despite the same thermal conductivity of the two greases, Ga grease always has the highest temperature (approximately 45.5 °C) under the same thermal shock because it has no effective phase–change to absorb heat above 30 °C (the lower limit of the service temperature). Similar to the continuous phase transition above 30 °C, TM grease exhibits a lower temperature increase (approximately 40.0 °C) under the transiently thermal shock. To characterize the thermal stability of the TM, 100 heating and cooling cycles were performed by DSC. All 100 cycles of the DSC curves are summarized in *SI Appendix*, Fig. S26, which shows nearly the same patterns and melting behaviors, indicating the high stability of the TMs. Furthermore, the first, 20th, 40th, 60th, 80th, and 100th cycle of the DSC cyclic curves are exhibited in one figure (*SI Appendix*, Fig. S27) to clearly show the same melting behaviors without phase separation, again indicating the phenomenal stability of the system. As a result, fluidic TM–based ESMs not only have similar excellent fluidity and high thermal conductivity as liquid metal, but they also provide high effective latent heat, continuous phase transition, and the ability to overcome the risk of leakage, which can solve a series of issues of traditional thermally conductive PCMs.

The prepared TM grease is successfully used in daily electronics and shows remarkable performance as an advanced ESM. Note that to the method for applying the grease is important to evaluate the thermal performance of the materials. Therefore, we used a 3—dimensional printer to fabricate two frames with fixed dimensions (*SI Appendix*, Fig. S28). The frames were used as molds to ensure the same geometry and volume of the thermal grease applied on the surface of the electronics. According to Fourier's law (Q/t = κAΔT/d, where Q is the heat from the source, t is time, κ is the thermal conductivity, d is the distance of heat
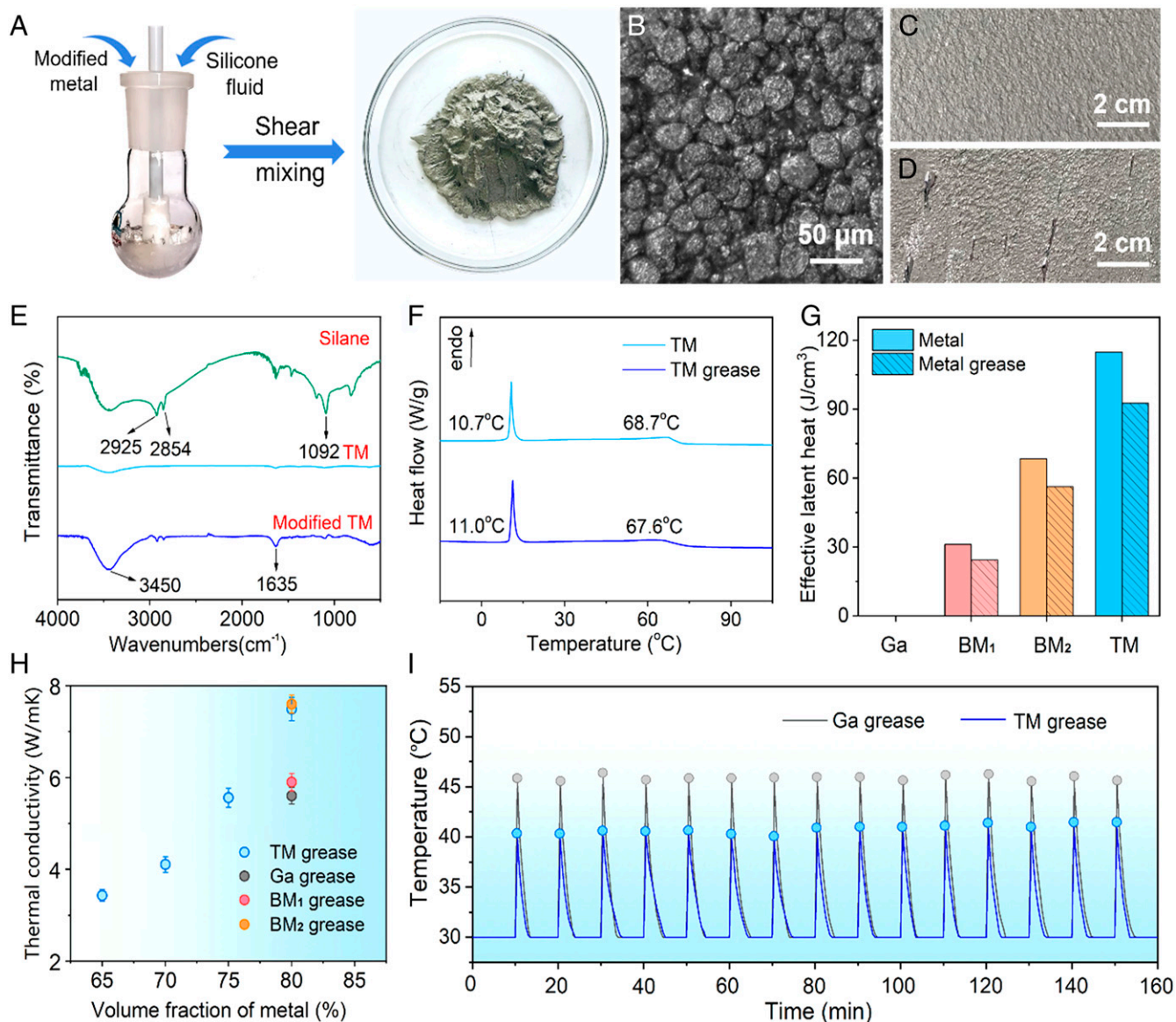
Fig. 3. Thermal grease from TMs. (*A*) The preparation of TM–based thermal grease. The modified TM and silicone oil are shear-mixed above the liquidus temperature (70 °C) of the metal. The photograph is the thermal grease with 80 vol% TM ($Ga_{0.20}In_{0.46}Sn_{0.34}$). (*B*) Scanning electron microscopy (SEM) image for TM grease (Scale bar, 50 μm). Photographs of (*C*) TM grease and (*D*) Ga-based grease coated on an aluminum plate (Scale bar, 2 cm). (*E*) FT-IR spectra of silane coupling agent (hexadecyl trimethoxysilane), TM, and modified TM. The samples were washed by ethanol 3 times before characterization. (*F*) DSC curves for TM and TM grease. (*G*) Enthalpy of fusion for different metals and their corresponding thermal grease in the service temperature window (above 30 °C). BM_1 and BM_2 are $Ga_{0.82}Sn_{0.18}$ and $Ga_{0.50}In_{0.50}$, respectively. (*H*) Thermal conductivity for TM grease with different TM volume fractions, Ga grease, BM_1 grease, and BM_2 grease. (*I*) Temperature of 80 vol% Ga greases and 75 vol% TM grease (0.5 mL) under the same thermal shock for 15 cycles. Thermal shock is controlled by heating the grease for 30 s at the same power (a 2.2 W mantle) and then naturally cooled, which can simulate common operations of electronics. The thermal shock tests are repeated for 15 cycles to estimate the stability of thermal management. Grey and blue dots corresponds to the peak temperature of the system with gallium grease and TM grease, respectively.

conduction (thickness of the grease), A is the contact area, and △T is the steady temperature difference), the Q/t will be constant for a certain device. Under steady state, the A/d value of the applied grease heavily determines the thermal performance (temperature difference, △T). The mold here is to eliminate the difference of A/d values of the utilized grease. To verify the impact from the geometry on the thermal performance of the applied grease, the two frames with the same A (inner size: 14 mm × 14 mm) but different d values (0.5 mm vs. 1 mm) were used to coat the same 75 vol% TM grease on the LED. *SI Appendix*, Fig. S29 shows that the LED with the smaller d value (0.5 mm) of the grease is approximately 12 °C lower than that of the LED with the higher d value (1 mm). This result confirms the significant impact on the thermal performance from the A/d values.

The mold (14 mm × 14 mm × 1 mm) was utilized to ensure the same thermal resistance of the applied grease for the correct evaluation of effects from the latent heat. Next, 0.2 mL 75 vol% TM grease and 80 vol% Ga grease was applied by the mold. The two greases have nearly the same thermal conductivity (Fig. 3*H*). The infrared images and temperature curves (Fig. 4 *A* and *B* and Movies S1–S3) showed that under the same applied conditions, the TM grease will retard the increasing temperature rate with time for the LED instead of changing the final temperatures. However, the temperature of the LED without ESMs immediately reached approximately 120 °C after the power was on for 150 s. The LED coated with 75 vol% TM grease showed a slower temperature increase, approximately 60 seconds, compared with the LED coated with Ga grease (Fig.

4B). The maximum temperature difference in the initial 60 seconds between the LEDs coated with TM grease and Ga grease could be approximately 8 °C (44 °C vs. 52 °C). In addition, the thermal management of a flashing LED by the TM grease was also characterized. The flashing LED (power at 3 W) can be turned on for 10 seconds and then cooled for 50 seconds. The flashing LEDs were coated with 0.2 mL Ga grease and TM grease by the mold. As in *SI Appendix*, Fig. S31, the results showed that the TM grease can retard the temperature increase of the flashing LED and show an approximately 5 °C lower peak temperature compared with that of the LED with Ga grease. This result indicates that TM grease with continuous phase transitions can prevent a sharp temperature increase and lower the peak temperature of the device. In these experiments, it should be stressed that Ga in the grease is in a supercooled state as confirmed by the DSC curve (*SI Appendix*, Fig. S30), which did not provide latent heat to cool the device. In contrast, the limited supercooling effects of TM and BM (39) indicate that compared with supercooling Ga, the BMs and TMs have stable phase transitions for readily thermal management in electronics.

Note that most electronics work transiently, which means that CPUs in personal computers and cell phones are usually in standby mode but experiece high temperatures only when heavy tasks are processing. Therefore, we evaluated the thermal
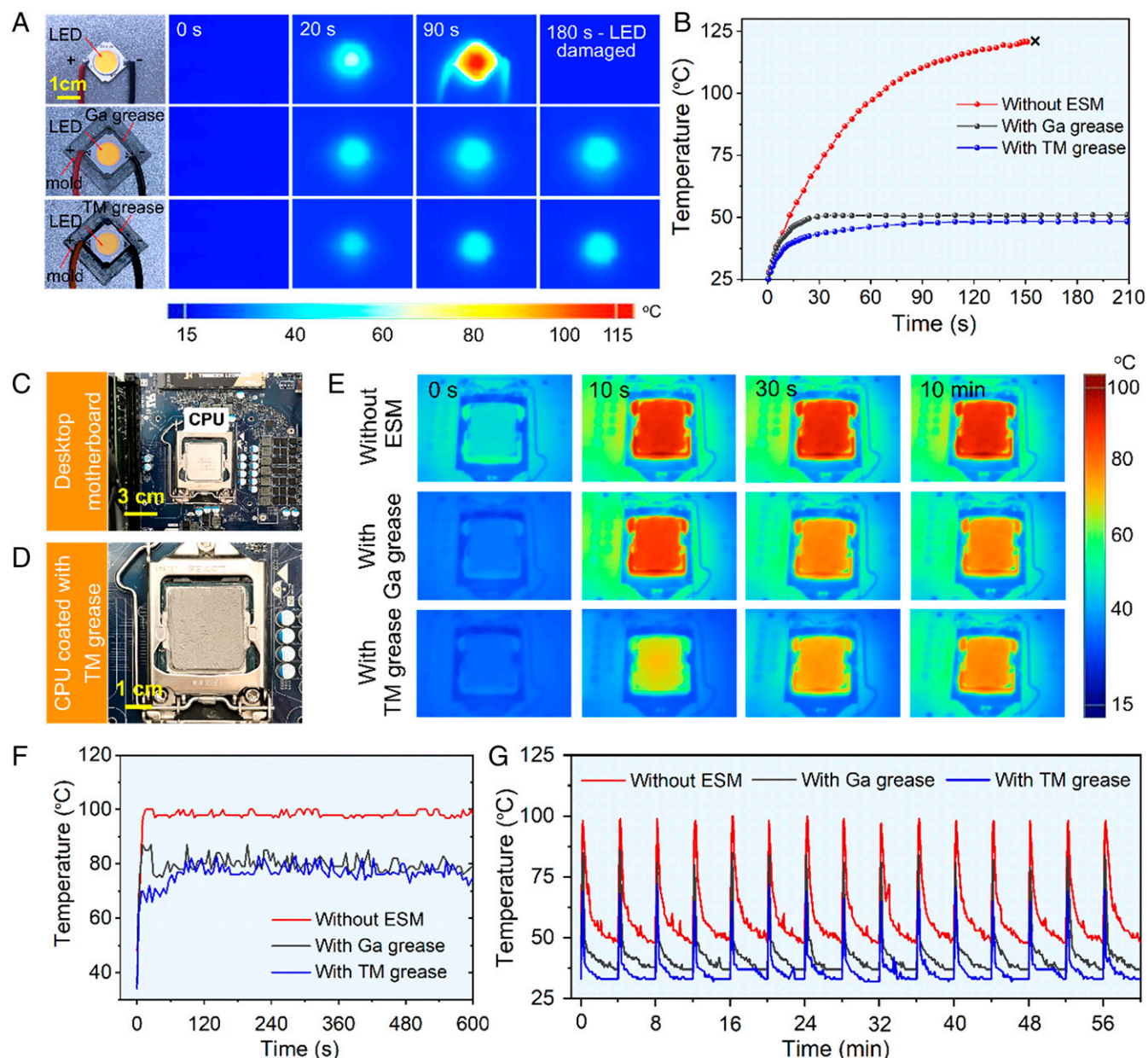
Fig. 4. Performance of TM grease in daily electronics. (*A*) Photographs of (*Top*) LED (power: 3W) without coating any ESMs, LED coated with 0.2 mL 80 vol% Ga grease (*Middle*) and LED coated with 0.2 mL 75 vol% TM grease (*Bottom*) and their corresponding infrared images to monitor the temperature change when working (Scale bar, 1 cm). Both greases were applied by the mold (14 mm × 14 mm × 1 mm). (*B*) The temperature–time curve for the working LED with different ESMs. An LED without ESM is damaged due to overheating after 154 seconds. (*C*) Photograph for a motherboard from a desktop computer. The center unit is a CPU (Intel Core i7-11700). (*D*) Photograph of the CPU coated with TM grease. (*E* and *F*) Infrared images of the CPU without ESM (*Top*), CPU coated with 0.46 mL 80vol% Ga grease (*Middle*), and CPU coated with 0.46 mL 75 vol% TM grease (*Bottom*) when the CPU ran at 100% usage. The thickness of both greases was controlled at 0.5 mm. The real-time temperature of the CPU was monitored (*F*). (*G*) The real-time temperature responses of a working CPU coated with the above greases upon instantaneous thermal shock for 15 cycles. The thermal shock is controlled when the CPU suddenly runs at 100% usage for 10 s and then stops to simulate the instantaneous heat flux of running large-scale software.

performance of TM grease in CPUs (Fig. 4 *C* and *G*). As shown in Fig. 4 *C* and *D*, 0.46 mL Ga grease and TM grease were carefully applied with the same thickness (0.5 mm). Fig. 4 *E* and *F* and *SI Appendix*, Fig. S32 exhibit the infrared photos and real-time temperature curves of the CPU running at 100% usage for 10 min. The CPU without grease showed the highest temperature, near 100 °C, when it was running. In contrast, the CPU coated with Ga grease showed a sharp temperature increase from approximately 37 °C to 86 °C in 10 s. Due to the overheating protection of the CPU itself, the CPU automatically engaged protective downclocking to lower the temperature to 75 °C and then finally stabilized at 81 °C. However, for the CPU coated with TM grease, the temperature of the CPU increased from approximately 34 °C to 68 °C in the initial 30 s instead of rising quickly to a high temperature, and it then stabilized at nearly 80 °C in 2 min. The results show that although the CPU coated with Ga grease and TM grease had nearly the same steady temperature, coating with TM grease will lead to a slower temperature increase as well as a lower peak temperature during transient operation. Continuous latent heat is critical to protect consumer electronics from thermal damage. Fig. 4*G* and *SI Appendix*, Fig. S33 exhibit the thermal shock results for the CPU in transient working conditions (that is, the CPU ran a large software program to reach 100% usage of the CPU intermittently for 10 s and then resting to simulate the instantaneous large heat flux). Since the TM grease has the phase transition to retard the temperature increase, the temperature of the CPU will not increase to a high level in a short time. For 80 vol% Ga grease, the peak temperature is approximately 17 °C higher than that of 75 vol% TM grease (average 84 °C vs. 67 °C), indicating the excellent thermal management of TM grease for the electronics.

Conclusion

In summary, this work brings the knowledge of the classic ternary phase transitions of metals into the field of ESMs, providing a powerful and universal strategy toward high-performance ESMs. The TMs successfully address the critical issues in traditional PCMs, showing excellent environmental adaptability, continuous phase transition, high thermal conductivity, and remarkably effective latent heat. This work offers a universal and theoretically predictable method to work with different metals, not confined to Ga-In-Sn, to adapt with various industrial systems. The phase–change thermal grease based on fluidic TM is also conveniently fabricated. TM grease shows excellent performance as an ESM for daily electronics (LEDs and computer CPUs) regarding thermal shock characterizations. This work should have a broad and significant impact in the field of thermal industry, electronics, and energy materials.

Materials and Methods

Materials. Ga (melting point at 29.8 °C), In (melting point at 157 °C), and Sn (melting point at 232 °C) were purchased from the Shenyang Jiabei commercial trading company. Silicone oil (DOW PMX-200) was obtained from Dongguan Tianying Craft Material. DOW TC-5888 was purchased from Jikewenkong in Taobao. LED (3W) was purchased from the Zhongshan Qianfang Lighting Technology Co. The motherboard (Intel H470) and CPU (Intel Core i7-11700) were purchased from the ASUS flagship store.

Preparation of TM. The metals Ga, In, and Sn (e.g., 3.49 g Ga, 13.20 g In, and 10.09 g Sn used to prepare $Ga_{0.20}In_{0.46}Sn_{0.34}$) were put into a 25 mL round-bottom flask and heated in a heating mantle at approximately 250 °C until melted. The mixtures were mechanically stirred at 500 revolutions per min for 60 s to mix the three metals. Finally, the Ga-In-Sn TM was obtained by cooling the mixture at room temperature. The entire preparation process was protected by N to prevent metal oxidation.

Step–cooling experiment for Ga, BM, and TM. In order to clearly understand the phase–transition processes of Ga, BM, and TM and to determine their specific phase–transition temperature, step–cooling experiments for Ga, BM ($Ga_{0.50}In_{0.50}$), and TM ($Ga_{0.40}In_{0.28}Sn_{0.32}$) were performed. Samples were obtained by first placing 2 mL molten metal in an elastomer container and then sealing them except for where the temperature probe was inserted. Finally, the samples were cooled at −18 °C. The temperature was recorded, and the graph of the temperature variation with time was plotted to analyze the phase transitions. The temperature corresponding to the turning point in the curve was the phase–transition temperature of the metal.

Thermal shock experiment. To evaluate the ability of different thermal greases to withstand thermal shock, thermal shock experiments for Ga grease, BM_1 ($Ga_{0.82}Sn_{0.18}$) grease, BM_2 ($Ga_{0.50}In_{0.50}$) grease, and TM ($Ga_{0.20}In_{0.46}Sn_{0.34}$) grease were performed. The sample was prepared by encapsulating 0.5 mL thermal grease in an elastomeric container with a copper tab on one side for contact with the power supply and a hole on the other side for inserting a temperature probe. Thermal shock was controlled by heating the sample for 30 seconds at the same power (2.2 W) and then naturally cooling it, which can simulate common operations in electronics. The thermal shock tests were repeated for 15 cycles to estimate the stability of thermal management.

Data Availability. All study data are included in the article and/or *SI Appendix*.

Author affiliations: ᵃSchool of Chemistry and Chemical Engineering, Jiangsu Hi-Tech Key Laboratory for Biomedical Research, Southeast University, Nanjing 211189, PR China

1. J. Song, X. Feng, Y. Huang, Mechanics and thermal management of stretchable inorganic electronics. *Natl. Sci. Rev.* **3**, 128–143 (2016).
2. Z. Ling *et al.*, Review on thermal management systems using phase change materials for electronic components, Li-ion batteries and photovoltaic modules. *Renew. Sustain. Energy Rev.* **31**, 427–438 (2014).
3. R. Cao *et al.*, Suppressing thermal negative effect and maintaining high-temperature steady electrical performance of triboelectric nanogenerators by employing phase change material. *ACS Appl. Mater. Interfaces* **13**, 41657–41668 (2021).
4. Y. Shi *et al.*, Functional soft composites as thermal protecting substrates for wearable electronics. *Adv. Funct. Mater.* **29**, 1905470 (2019).
5. J. Chen, X. Huang, B. Sun, P. Jiang, Highly thermally conductive yet electrically insulating polymer/boron nitride nanosheets nanocomposite films for improved thermal management capability. *ACS Nano* **13**, 337–345 (2019).
6. Y. Lu *et al.*, Novel smart textile with phase change materials encapsulated core-sheath structure fabricated by coaxial electrospinning. *Chem. Eng. J.* **355**, 532–539 (2019).
7. J. Yang *et al.*, High-performance composite phase change materials for energy conversion based on macroscopically three-dimensional structural materials. *Mater. Horiz.* **6**, 250–273 (2019).
8. X. Chen *et al.*, Smart integration of carbon quantum dots in metal-organic frameworks for fluorescence-functionalized phase change materials. *Energy Storage Mater.* **18**, 349–355 (2019).
9. H. Song *et al.*, Two-dimensional materials for thermal management applications. *Joule* **2**, 442–463 (2018).
10. M. M. Waldrop, The semiconductor industry will soon abandon its pursuit of Moore's law. Now things could get a lot more interesting. *Nature* **530**, 144–147 (2016).
11. K. Ruan, Y. Guo, J. Gu, Liquid crystalline polyimide films with high intrinsic thermal conductivities and robust toughness. *Macromolecules* **54**, 4934–4944 (2021).
12. W. Aftab *et al.*, Phase change material-integrated latent heat storage systems for sustainable energy solutions. *Energy Environ. Sci.* **14**, 4268–4291 (2021).
13. S. Wu *et al.*, High-performance thermally conductive phase change composites by large-size oriented graphite sheets for scalable thermal energy harvesting. *Adv. Mater.* **31**, e1905099 (2019).
14. Y. Han, K. Ruan, J. Gu, Janus (BNNS/ANF)-(AgNWs/ANF) thermal conductivity composite films with superior electromagnetic interference shielding and Joule heating performances. *Nano Res.* **15**, 4747–4755 (2022).
15. Y. Lin, Y. Jia, G. Alva, G. Fang, Review on thermal conductivity enhancement, thermal properties and applications of phase change materials in thermal energy storage. *Renew. Sustain. Energy Rev.* **82**, 2730–2742 (2018).
16. Z. Ling *et al.*, Thermal conductivity of an organic phase change material/expanded graphite composite across the phase change temperature range and a novel thermal conductivity model. *Energy Convers. Manage.* **102**, 202–208 (2015).
17. K. Yuan *et al.*, Engineering the thermal conductivity of functional phase-change materials for heat energy conversion, storage, and utilization. *Adv. Funct. Mater.* **30**, 1904228 (2020).
18. B. Wang, G. Li, L. Xu, J. Liao, X. Zhang, Nanoporous boron nitride aerogel film and its smart composite with phase change materials. *ACS Nano* **14**, 16590–16599 (2020).

19. J. A. Rogers, Wearable electronics: Nanomesh on-skin electronics. *Nat. Nanotechnol.* **12**, 839–840 (2017).
20. S. Pan, J. Ren, X. Fang, H. Peng, Integration: An effective strategy to develop multifunctional energy storage devices. *Adv. Energy Mater.* **6**, 1501867 (2016).
21. C. Tan *et al.*, A high performance wearable strain sensor with advanced thermal management for motion monitoring. *Nat. Commun.* **11**, 3530–3540 (2020).
22. A. L. Moore, L. Shi, Emerging challenges and materials for thermal management of electronics. *Mater. Today* **17**, 163–174 (2014).
23. S. Niu *et al.*, A wireless body area sensor network based on stretchable passive tags. *Nat. Electron.* **2**, 361–368 (2019).
24. P. J. Shamberger, N. M. Bruno, Review of metallic phase change materials for high heat flux transient thermal management applications. *Appl. Energy* **258**, 113955 (2020).
25. H. Ge, H. Li, S. Mei, J. Liu, Low melting point liquid metal as a new class of phase change material: An emerging frontier in energy area. *Renew. Sustain. Energy Rev.* **21**, 331–346 (2013).
26. X. Ge *et al.*, Low melting-point alloy-boron nitride nanosheet composites for thermal management. *ACS Appl. Nano Mater.* **3**, 3494–3502 (2020).
27. M. D. Dickey, Stretchable and soft electronics using liquid metals. *Adv. Mater.* **29**, 1606425 (2017).
28. Y. Lin, J. Genzer, M. D. Dickey, Attributes, fabrication, and applications of gallium-based liquid metal particles. *Adv. Sci. (Weinh.)* **7**, 2000192 (2020).
29. T. Daeneke *et al.*, Liquid metals: Fundamentals and applications in chemistry. *Chem. Soc. Rev.* **47**, 4073–4111 (2018).
30. S. V. Garimella, L.-T. Yeh, T. Persoons, Thermal management challenges in telecommunication systems and data centers. *IEEE Trans. Compon. Packaging Manuf. Technol.* **2**, 1307–1316 (2012).
31. C. Macris, R. G. Ebel, US Patent 7755184 (2010). C. Macris, R. G. Ebel, Liquid metal thermal interface material system, US Patent 7755184B2 (2010).
32. X. Hu *et al.*, Multiscale disordered porous fibers for self-sensing and self-cooling integrated smart sportswear. *ACS Nano* **14**, 559–567 (2020).
33. M.-T. F. Rodrigues *et al.*, A materials perspective on Li-ion batteries at extreme temperatures. *Nat. Energy* **2**, 17108 (2017).
34. Q. Ren, P. Guo, J. Zhu, Thermal management of electronic devices using pin-fin based cascade microencapsulated PCM/expanded graphite composite. *Int. J. Heat Mass Transf.* **149**, 19199 (2020).
35. S. Y. Tang *et al.*, Phase separation in liquid metal nanoparticles. *Matter* **1**, 192–204 (2019).
36. M. C. Flemings, Solidification processing. *Mater. Trans.* **5**, 2121–2135 (1974).
37. M. C. Flemings, Behavior of metal alloys in the semisolid state. *Metall. Mater. Trans. A-Phys.* **22**, 957–982 (1991).
38. T. J. Anderson, I. Ansara, The Ga-In (gallium-indium) system. *J. Phase Equilibria* **12**, 64–73 (1991).
39. H. Liu *et al.*, Stimuli-driven insulator-conductor transition in a flexible polymer composite enabled by biphasic liquid metal. *Adv. Mater.* **33**, e2104634 (2021).
40. D. R. F. West, *Ternary Equilibrium Diagrams* (Springer, London, UK, 1982).
41. D. Zivkovic, D. Manasijevic, Z. Zivkovic, Thermodynamic study of Ga-Sn and Ga-Zn systems using quantitative differential thermal analysis. *J. Therm. Anal. Calorim.* **74**, 85–96 (2003).
42. S. C. Harris, Microwave studies of superconducting 2-phase In-Sn. *Proc. R. Soc. Lond. A Math. Phys. Sci.* **350**, 267–279 (1976).
43. J. L. F. Goldstein, J. W. Morris, The effect of substrate on the microstructure and creep of eutectic In-Sn. *Metall. Mater. Trans., A Phys. Metall. Mater. Sci.* **25**, 2715–2722 (1994).
44. S. Chen, H.-Z. Wang, R.-Q. Zhao, W. Rao, J. Liu, Liquid metal composites. *Matter* **2**, 1446–1480 (2020).
45. H. Liu *et al.*, Liquid metal gradient fibers with reversible thermal programmability. *Mater. Horiz.* **7**, 2141–2149 (2020).
46. K. Ruan *et al.*, Significant reduction of interfacial thermal resistance and phonon scattering in graphene/polyimide thermally conductive composite films for thermal management. *Research (Wash D C)* **2021**, 8438614 (2021).
47. X. Y. Huang *et al.*, Polyhedral oligosilsesquioxane-modified boron nitride nanotube based epoxy nanocomposites: An ideal dielectric material with high thermal conductivity. *Adv. Funct. Mater.* **23**, 1824–1831 (2013).
48. L. Hu *et al.*, Preparation and properties of fluorinated silicon two-component polyurethane hydrophobic coatings. *Polym. Int.* **69**, 448–456 (2020).
49. J. Yan, Y. Lu, G. Chen, M. Yang, Z. Gu, Advances in liquid metals for biomedical applications. *Chem. Soc. Rev.* **47**, 2518–2533 (2018).
50. R. Tutika, S. H. Zhou, R. E. Napolitano, M. D. Bartlett, Mechanical and functional tradeoffs in multiphase liquid metal, solid particle soft composites. *Adv. Funct. Mater.* **28**, 804336 (2018).
51. M. D. Bartlett *et al.*, High thermal conductivity in soft elastomers with elongated liquid metal inclusions. *Proc. Natl. Acad. Sci. U.S.A.* **114**, 2143–2148 (2017).